Article:
Haruna, A.B., Podile, S., Seotsanyana-Mokhosi, I. et al. (2025) Synergistic effects of microwave irradiation and CeF3 surface coating of lithium titanate for stable, high-capacity, and high-rate lithium-ion batteries. Energy Advances. ISSN: 2753-1457

https://doi.org/10.1039/d5ya00303b

Energy Advances

ROYAL SOCIETY OF CHEMISTRY

PAPER

View Article Online
View Journal

Cite this: DOI: 10.1039/d5ya00303b

Synergistic effects of microwave irradiation and CeF_3 surface coating of lithium titanate for stable, high-capacity, and high-rate lithium-ion batteries

Aderemi B. Haruna,[a] Seromo Podile,[a] Itumeleng Seotsanyana-Mokhosi,[a] Thapelo Mofokeng,[a] Alexander Roberts,[b] Jennifer Johnstone-Hack,[c] Paul Shearing[def] and Kenneth I. Ozoemena *[a]

The low theoretical specific capacity and rapid capacity degradation, especially during long cycling, have been the key challenges to the practical application of lithium titanate ($Li_4Ti_5O_{12}$) as an anode material for stable, high-energy and high-power density lithium-ion batteries (LIBs). This study reports a novel strategy of the synergy of surface lattice plane engineering by microwave irradiation and CeF_3 surface coating to synthesize a high-specific-capacity, high-rate and durable LTO–CeF_3–mw anode material for LIBs. The innovative anode material shows outstanding specific capacity, rate capability and long-term cycle stability. It is of interest to note that the LTO–CeF_3–mw anode material has a specific capacity of 191.1 mAh g^{-1} at 175 mA g^{-1} (1C), which is greater than the theoretical specific capacity of LTO (175 mAh g^{-1}). Furthermore, LTO–CeF_3–mw has specific capacities of 168.3 and 119.9 mAh g^{-1} at 875 mA g^{-1} (5C) and 1750 mA g^{-1} (10C), respectively. Remarkably, it shows a specific capacity of 166.5 mAh g^{-1} after 1000 cycles at 5C and a capacity retention of 98.9%. This notable electrochemical performance of LTO–CeF_3–mw is attributed to the synergy of surface lattice plane engineering by microwave irradiation and CeF_3 surface coating that transformed the surface lattice plane (111) of LTO to (220) and (310) in LTO–CeF_3–mw, resulting in high surface area which significantly improved mass transport. Therefore, the unique structure of the LTO–CeF_3–mw anode material is a key development for achieving safe, durable, high-energy and high-power lithium-ion batteries, with potential applications in large-scale energy storage.

Received 17th October 2025,
Accepted 19th December 2025

DOI: 10.1039/d5ya00303b

rsc.li/energy-advances

1. Introduction

Spinel lithium titanate, $Li_4Ti_5O_{12}$ (LTO), has been considered the preferred alternative to the current state-of-the-art graphite anode material for lithium-ion batteries (LIBs). This is because of its great advantages, which include its flat high working voltage (~1.55 V *versus* Li/Li^+), which is above the reduction potential of most organic electrolytes. Therefore, the formation of a solid electrolyte interphase (SEI) and lithium dendrites can be suppressed, enhancing the safety of lithium-ion batteries.[1,2] Furthermore, LTO shows negligible volume change (zero strain) during lithium insertion and extraction, which leads to excellent cyclability and safety.[3] Unfortunately, LTO has not been widely used in practical applications because it has a low theoretical capacity (175 mA h g^{-1}),[3] poor capacity at high C-rates because of its inherent low electronic conductivity and poor Li^+ diffusion coefficient,[4–6] and capacity degradation during long cycling charge–discharge process.[7] There have been several strategies reported to mitigate these drawbacks,[6,8–13] and of these strategies, the introduction of Ti^{3+} is the most reported.[14–26] The LTO (Ti^{4+}) has poor electronic conductivity because of its empty 3d electronic orbital ($3d^0$) and poor ionic conductivity because of its small ionic size. The partial reduction of Ti^{4+} to Ti^{3+} to form Ti^{3+}–O–Ti^{4+} pairs in LTO has been reported to enhance the electron conductivity of LTO *via* the Ti^{3+} having electronic configuration $[Ar]3d^1$.[16,17,22] However, Aurbach *et al.*[27] reported that Ti^{4+} is the most stable oxidation state of Ti. Ti^{4+} is very stable because of its completely filled 3p orbital, while Ti^{3+} is less stable because it has one

[a] Molecular Sciences Institute, School of Chemistry, University of the Witwatersrand, Johannesburg 2050, South Africa. E-mail: Kenneth.ozoemena@wits.ac.za
[b] Centre for E-Mobility and Clean Growth, Coventry University, Coventry CV1 2TL, UK
[c] School of Chemical, Materials and Biological Engineering, Sir Robert Hadfield Building, The University of Sheffield, Mappin Street, Sheffield S1 3JD, UK
[d] Department of Engineering Science, University of Oxford, Parks Road, Oxford OX1 3PJ, UK
[e] Electrochemical Innovation Lab, Department of Chemical Engineering, University College London, London WC1E 7JE, UK
[f] The ZERO Institute, University of Oxford, Oxford OX2 0ES, UK

electron in its 3d orbital ($3d^1$). Therefore, this research work used simple microwave irradiation and CeF_3 surface modification to strategically modify the commercial LTO to retain its more stable Ti^{4+} without the introduction of the conventional conductive Ti^{3+}. The uniqueness of this study is the synergistic modification strategy that retained the Ti^{4+} and still enhanced the specific capacity and capacity retention of the modified microwave-coated sample.

In this work, CeF_3 was used to surface-modify LTO because of its high ionic conductivity and structural stability.[28] CeF_3 surface-modified LTO has a better stability in $LiPF_6$ electrolyte compared to metal oxides that have lattice oxygen that can produce water which reacts with the $LiPF_6$ salt to produce HF that leads to side reactions. CeF_3 was first used to surface-modify LTO (to obtain a product denoted as LTO–CeF_3) and subsequently subjected to microwave irradiation (to obtain a product denoted as LTO–CeF_3–mw). Both processes were aimed at strategically maintaining the Ti^{4+} and introducing substitutional (point) defects into the commercial LTO.

This study showed that the strategy introduced led to significant surface lattice plane transformation and point defects. The LTO–CeF_3–mw exhibited larger *d*-spacing than its counterparts investigated in this work. Such lattice expansion is advantageous for smooth Li^+ diffusion and thus improves the ionic conductivity. To the best of our knowledge, this is the first time that microwave irradiation and CeF_3 have been used to fine-tune the physico-chemical properties of the LTO anode for improved electrochemical performance (in terms of cycling stability, increased specific capacity, and high rate capability).

2. Experimental section

2.1 Synthesis of LTO–CeF_3, LTO–m and LTO–CeF_3–m

Ammonium fluoride NH_3F and cerium nitrate hexahydrate $Ce(NO_3)_3{\cdot}6H_2O$ were each dissolved in distilled water. Thereafter, LTO powder (Shandong Gelon LIB Co., Ltd China) was submerged and stirred inside the cerium nitrate hexahydrate solution. The ammonium fluoride solution was steadily added to the resulting LTO and cerium nitrate hexahydrate solution. After a constant stir at 80 °C for 5 h, the resulting powder was filtered using a centrifuge. The filtered powder was then calcinated at 400 °C for 5 h in an argon atmosphere. This synthesis method is illustrated in Fig. 1a. The ammonium fluoride and cerium nitrate hexahydrate made a stoichiometric molar ratio of $Ce^{3+}/F^- = 1/3$, with the amount of CeF_3 corresponding to ~2 wt% of the LTO powders (based on previous reports of wt% coat of 1 and 2).[28–30] To synthesize microwaved materials, the LTO-p and CeF_3-coated LTO were subjected to microwave radiation at 600 watts for 20 min[31] as shown in Fig. 1b.

2.2 Physical characterizations

Bruker D2 phaser is used to determine the XRD of the materials, and the instrument was operated using Cu-Kα radiation at 30 kV

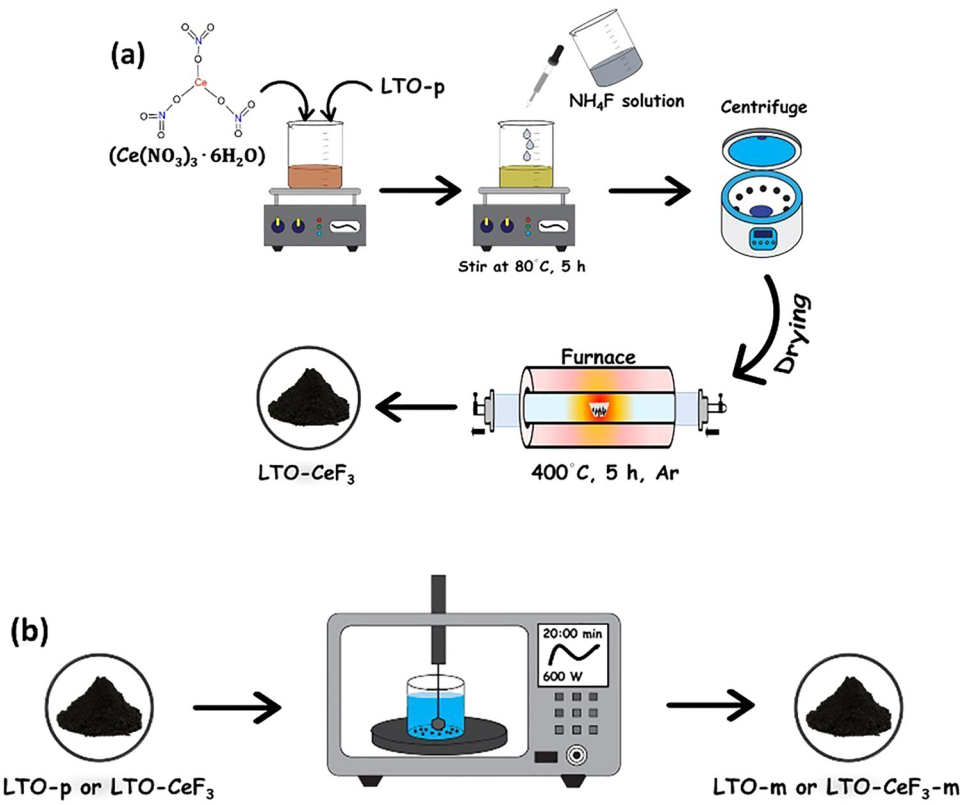

Fig. 1 Schematic of synthesis methods of (a) LTO–CeF_3 and (b) LTO–mw and LTO–CeF_3–mw.

and 10 mA. A Micromeritics Tristar 3000 BET instrument was used to determine the pore sizes of the materials. The samples were degassed at 150 °C for 4 h, with gas adsorption performed in liquid nitrogen (−195 °C). A thermogravimetric analyzer (PerkinElmer 6000) was used to determine how stable and versatile the materials were. The morphological and structural properties of the synthesized materials were determined using HRTEM (JEOL JEM 2100) at 200 Kv; samples were dissolved in ethanol, sonicated for about 20 min and dispersed on a carbon-coated copper grid for analysis. XPS measurements were studied with ESCAlab 250Xi XPS having a monochromatic Al kα radiation source (1486.7 eV). Survey spectra were taken at a pass energy of 100 eV and a high-resolution pass energy of 20 eV. The 514.5 nm line of an argon-ion laser and a Horiba Jobin-Yvon LabRAM HR Raman spectrometer equipped with an Olympus BX41 microscope attachment were used to obtain the Raman spectra. The LabSpec v5 software was used to capture the data.

2.3 Electrochemical characterization

The LTO anodes were constructed with 85 wt% active material, 10 wt% carbon black (Super C45), 2.5 wt% CMC and 2.5 wt% SBR. Mixtures of an active material and carbon black were ground into a fine powder and slowly added to a liquid thickening agent in piles. A liquid thickening agent was made by stirring CMC and SBR in distilled water heated to 60 °C. The resulting well-mixed slurry was coated on a copper foil and dried at 105 °C for 12 h in a vacuum oven. The active mass loading of the 4 electrode materials is ∼2.0 mg on a 12 mm diameter disc. The electrochemical tests of all the samples were tested using a coin-type cell (CR 2032) assembled inside an argon-filled glove box. The cell comprised of the as-prepared working electrode, lithium foil as a counter electrode and grade GD 1UM, 47 mm Whatman paper as a separator. The electrolyte used was a 1 M $LiPF_6$ solution in ethylene carbonate (EC) : diethyl carbonate (DEC) : ethyl methylcarbonate (EMC) with a volume ratio of 1 : 1 : 1. The coin cells remained in the glovebox overnight before they were taken out for electrochemical measurements (CV: 1.0–2.5 V and galvanometry discharge: 1.0–2.5 V) using the BioLogic system (BCS-800 series) instrument.

3. Results and discussion

Fig. 2 compares the TEM images of the four materials. The images suggest that the pristine LTO is somewhat aggregated upon irradiation with microwaves (see LTO–mw). However, upon coating with the CeF_3, microwave irradiation leads to well-dispersed CeF_3 nanoparticles on the LTO. This is consistent with the SEM-EDS mapping (Fig. S1). The SEM-EDS revealed that the atomic % of Ce in LTO–CeF_3 and LTO–CeF_3–mw are 1.4 and 1.3%, respectively. The enhanced dispersion of CeF_3 nanoparticles on the LTO–CeF_3–mw suggests that it will give better Li-ion diffusion/transport kinetics and better protection of the LTO–CeF_3–mw electrode surface than others.

The HRTEM shows that LTO-p has lattice fringes with spacings of 0.486 nm and 0.493 nm in regions (I) and (II),

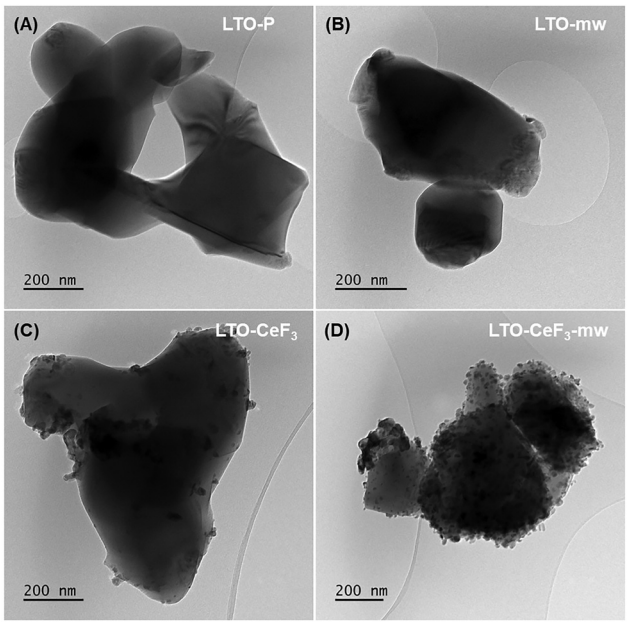

Fig. 2 TEM micrographs of (A) LTO-p, (B) LTO–mw, (C) LTO–CeF_3, and (D) LTO–CeF_3–mw.

respectively, as shown in Fig. S2. The observed spacing in these regions is attributed to the lattice plane (111) of the spinel $Li_4Ti_5O_{12}$ phase.[32] This confirms the existence of only $Li_4Ti_5O_{12}$ in the LTO-p sample. The selected area electron diffraction (SAED) patterns of regions (I) and (II), with all these regions being mono-crystalline, and this is seen through their discrete bright spots that are orderly arranged in a grid pattern.

It is pertinent to note that microwave irradiation introduced the LTO surface lattice planes (220), (310) and (222) in the microwave-irradiated sample LTO–mw, as shown in Fig. 3A. Rikarte *et al.*[33] reported a similar occurrence where the LTO surface plane (111) is transformed to surface plane (222) and anatase TiO_2 plane (101). The LTO–mw lattice planes (220), (222) and (310) have lattice fringe spacings of 0.280, (0.238 and 0240) and 0.267 nm, respectively. These lattice fringe spacings are assigned to the lattice planes using the "crystallographic information file (cif)" of $Li_4Ti_5O_{12}$. The SAED images of all the regions indicate the single crystalline nature of the cubic spinel.[34]

Fig. 3B shows that LTO–CeF_3 contains anatase TiO_2, CeF_3 and LTO, as demonstrated by lattice fringe spacings: 0.334 nm corresponding to the TiO_2 anatase (101) plane in region (I), 0.312 and 0.321 nm corresponding to the CeF_3 (111) plane in regions (II) and (III), respectively,[35] and 0.416 nm corresponding to the LTO (111) plane in region (IV).[36] The presence of TiO_2 in sample LTO–CeF_3 shows that CeF_3 might have not only physically covered the surface of the LTO but has chemically reacted with the LTO to produce the TiO_2, as in the chemical reaction in eqn (1). This implies that CeF_3 leads to both surface coating and bulk doping, which is a normal behaviour for its cousin CeO_2.

$$\underset{(\mathbf{LTO-p})}{Li_4\mathbf{Ti_5}O_{12}} + CeF_3 \xrightarrow[Ar]{400\ ^\circ C\ 5\ h} \underset{(\mathbf{LTO-CeF_3})}{Li_4\mathbf{Ti_{5-x}}Ce_xO_{12-y}F_y/Ti_xO_y} \quad (1)$$

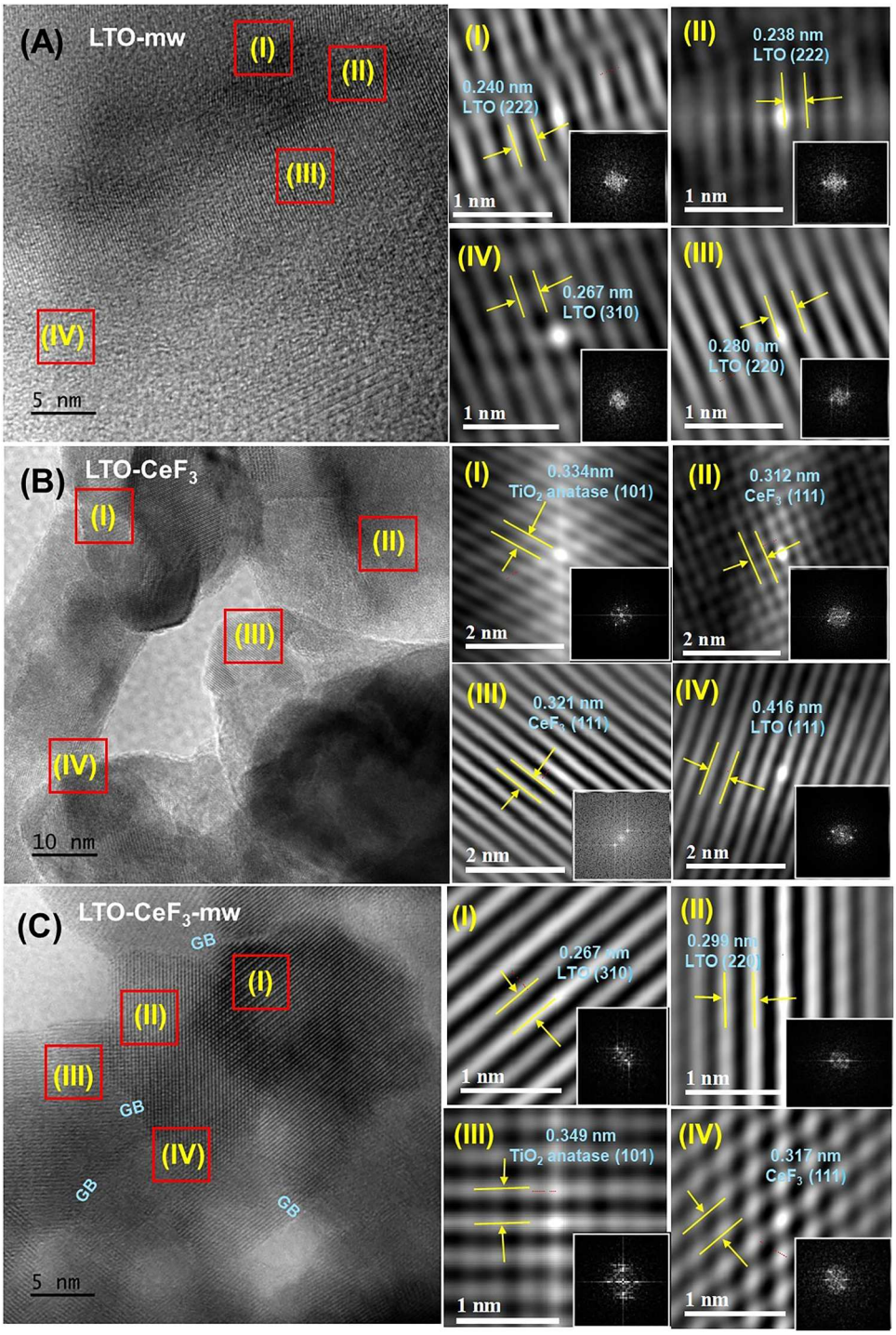

Fig. 3 HRTEM image of (A) LTO–mw, region (I): LTO (222) and SAED image of lattice plane, region (II): LTO (222) and SAED image of lattice plane, region (III): LTO (220) and SAED image of lattice plane and region (IV): LTO (310) and SAED image of lattice plane, (B) region (I): TiO_2 anatase (101) and SAED image of lattice plane, region (II): CeF_3 (111) and SAED image of lattice plane, region (III): CeF_3 (111) and SAED image of lattice plane and region (IV): LTO (111) and SAED image of lattice plane, (C) region (I): LTO (310) and SAED image of lattice plane, region (II): LTO (220) and SAED image of lattice plane, region (III): TiO_2 anatase (101) and SAED image of lattice plane and region (IV): CeF_3 (111) and SAED image of lattice plane.

Surface coating and doping have been common strategies for defect engineering in electrode materials such as LTO to improve their structure and surface properties for enhanced electrochemical performances. In this research work, the CeF_3 surface modification is used to introduce cation and anion lattice defects (Ce and F, respectively) into the LTO lattice structure. These lattice defects in the coated samples LTO–CeF_3 and LTO–CeF_3–mw are revealed in the HRTEM and XPS

Table 1 Lattice fringe spacings of the lattice planes of LTO, LTO–mw, LTO–CeF_3 and LTO–CeF_3–mw

Lattice plane	LTO (111)	LTO (111)	LTO (220)	LTO (222)	LTO (222)	LTO (310)	CeF_3 (111)	CeF_3 (111)	TiO_2
LTO-p (nm)	0.486	0.493							
LTO–mw (nm)			0.280	0.240	0.238	0.267			
LTO–CeF_3 (nm)	0.416						0.312	0.321	0.334
LTO–CeF_3–mw (nm)			0.299			0.267	0.317		0.349

analysis results below. The CeF_3-coated electrode samples are expected to give faster Li^+ kinetics in electrochemistry.

Furthermore, it is interesting to note that the LTO lattice plane (111) in the LTO–CeF_3 sample has a decreased lattice spacing of 0.416 nm compared to 0.486 nm in the LTO-p lattice plane (111) (Table 1). The observed SAED images indicate that anatase TiO_2 and CeF_3 have a mono-crystalline nature. Fig. 3C indicates that LTO–CeF_3–mw has LTO lattice planes (310) in region (I) and (220) in region (II) having lattice fringe spacings of 0.267 and 0.299 nm, respectively, while region (III) has the TiO_2 anatase lattice plane (101) with lattice fringe spacings of 0.349 nm and region (IV) has the CeF_3 lattice plane (111) with lattice fringe spacing of 0.317 nm. The SAED images of the regions on this sample are single crystalline. It can be concluded that the coated sample LTO–CeF_3 and microwave-irradiated coated sample LTO–CeF_3–mw have a dual-phase LTO–TiO_2 composite. LTO–CeF_3–mw also shows grain boundary (GB).

Table 1 shows that LTO–CeF_3–mw has lattice fringe spacing of 0.299 nm for lattice plane LTO (220) which is greater than that of LTO–mw: 0.280 nm. Furthermore, LTO–CeF_3–mw has larger lattice fringe spacing of 0.317 and 0.349 nm, respectively, for lattice planes CeF_3 (111) and TiO_2 (101) than that of LTO–CeF_3: CeF_3 (111) and TiO_2 (101) that has 0.312 and 0.334 nm, respectively. These lattice expansions of surface lattice planes LTO (220), CeF_3 (111) and TiO_2 are present because of the synergy between microwave irradiation and CeF_3 surface modification of the LTO-p.[37] These improved properties of the microwave-irradiated coated sample LTO–CeF_3–mw are because of the presence of the point defects that have better microwave irradiation absorption and thus resulted in higher heating rate and temperature than the stoichiometry Ti_5 of LTO–mw in the same microwave irradiation operation parameters.[38]

Fig. 4A shows Raman spectra of the four samples. All the materials contain Raman vibration modes at 236, 343, 429, 678, and 770 cm^{-1} which conform with the $A_{1g} + E_g + 3F_{2g}$ mode of the spinel LTO structure.[39] The vibration bands at 678 and 770 cm^{-1} resulted from the Ti–O stretch vibration of TiO_6 octahedra. The bands at 343 and 429 cm^{-1} are linked to the Li–O stretch vibration of LiO_4 or LiO_6 tetrahedral, and the 236 cm^{-1} band originates from O–Ti–O.[40,41] It is interesting to note that relative to the pristine sample (LTO-p), both the Ti–O and O–Ti–O vibration bands in LTO–mw, LTO–CeF_3 and LTO–CeF_3–mw did not show any shift. This shows that there is no change in the oxidation state of the Ti in the modified samples (all the samples have the oxidation state of Ti as +4, and there is no partial reduction of the Ti^{4+} to Ti^{3+}. Furthermore, it is pertinent to note that the coated samples (LTO–CeF_3 and LTO–CeF_3–mw) show an additional vibration peak at 143 cm^{-1}, which is attributed to anatase TiO_2.[42] Raman spectra show that the coated samples LTO–CeF_3 and LTO–CeF_3–mw have both anatase TiO_2 and spinel $Li_4Ti_5O_{12}$ vibration peaks, which confirm that LTO–CeF_3 and LTO–CeF_3–mw are dual-phase spinel $Li_4Ti_5O_{12}$–TiO_2 composites. This is consistent with the HRTEM results.

XPS surface composition analysis (Fig. 4B) shows that all the samples have two characteristic peaks at $\approx$458.0 and 463.8 eV which relate to the binding energy of Ti $2p_{3/2}$ and Ti $2p_{1/2}$ of Ti^{4+} in LTO.[43] It is intriguing to see that there is no obvious change in the Ti 2p spectra in the modified samples, and this provides evidence that there was no formation of Ti^{3+}. Furthermore, it is of interest to note that the spin–orbit splitting, *i.e.*, the change in energy between the Ti $2p_{3/2}$ and Ti $2p_{1/2}$ peaks ($\Delta E_{Ti\,2p} = E_{2p_{1/2}} - E_{2p_{3/2}}$) is 5.8 eV, which shows that Ti oxidation state is +4 (Ti^{4+}). These findings correlate with the Raman results. Fig. 4C shows the Ce 3d peaks of LTO–CeF_3 and LTO–CeF_3–mw in the range of 870 to 920 eV which confirms the presence of Ce in the CeF_3 surface-modified samples.

Crystallographic structures of the materials were evaluated using X-ray powder diffraction, as shown in Fig. 4E. All the diffraction peaks of the materials can be indexed to (111), (311), (400), (331), (333), (440), (531) and (533) of standard cubic spinel $Li_4Ti_5O_{12}$ (JCPDS Card No. 49-0207) with the *Fd*3*m* space group.[44,45] No additional reflection peaks are observed, indicating the absence of impurities and diffraction peaks associated with CeF_3 in the coated samples (LTO–CeF_3 and LTO–CeF_3–m) are not detected, which may be due to relatively low CeF_3 content ($\sim$2 wt%).[46] Also, this indicates that the microwave irradiation and CeF_3 surface modification do not change the spinel structure of the LTO. However, the lattice plane (111) is the most intense peak in the samples' diffraction patterns, which signifies that all four samples have normal spinel structures. The expanded (111) peak region (Fig. 4F) shows some interesting findings that should be emphasized. First, in the LTO–CeF_3, the peak (111) shifted to the higher 2θ degree position relative to that of the LTO-p. This indicates that there is lattice contraction in the coated sample LTO–CeF_3. This is consistent with the results of the HRTEM which show that there is a decrease in lattice spacing from 0.486 nm in LTO (111) of LTO-p to 0.416 nm in that of LTO–CeF_3. It is interesting to note that the lattice contracted instead of expanding, despite the introduction of Ce^{3+}, which has a larger ionic radius of 1.07 Å than that of Ti^{4+} (0.605 Å). The lattice contraction in LTO–CeF_3 may have occurred because the bond strength of Ce–O is greater than that of Ti–O in the octahedral site, and the Ce–O has higher octahedral site preference energies (OPE) than Ti–O which results in a decrease in the bond length.[47,48]

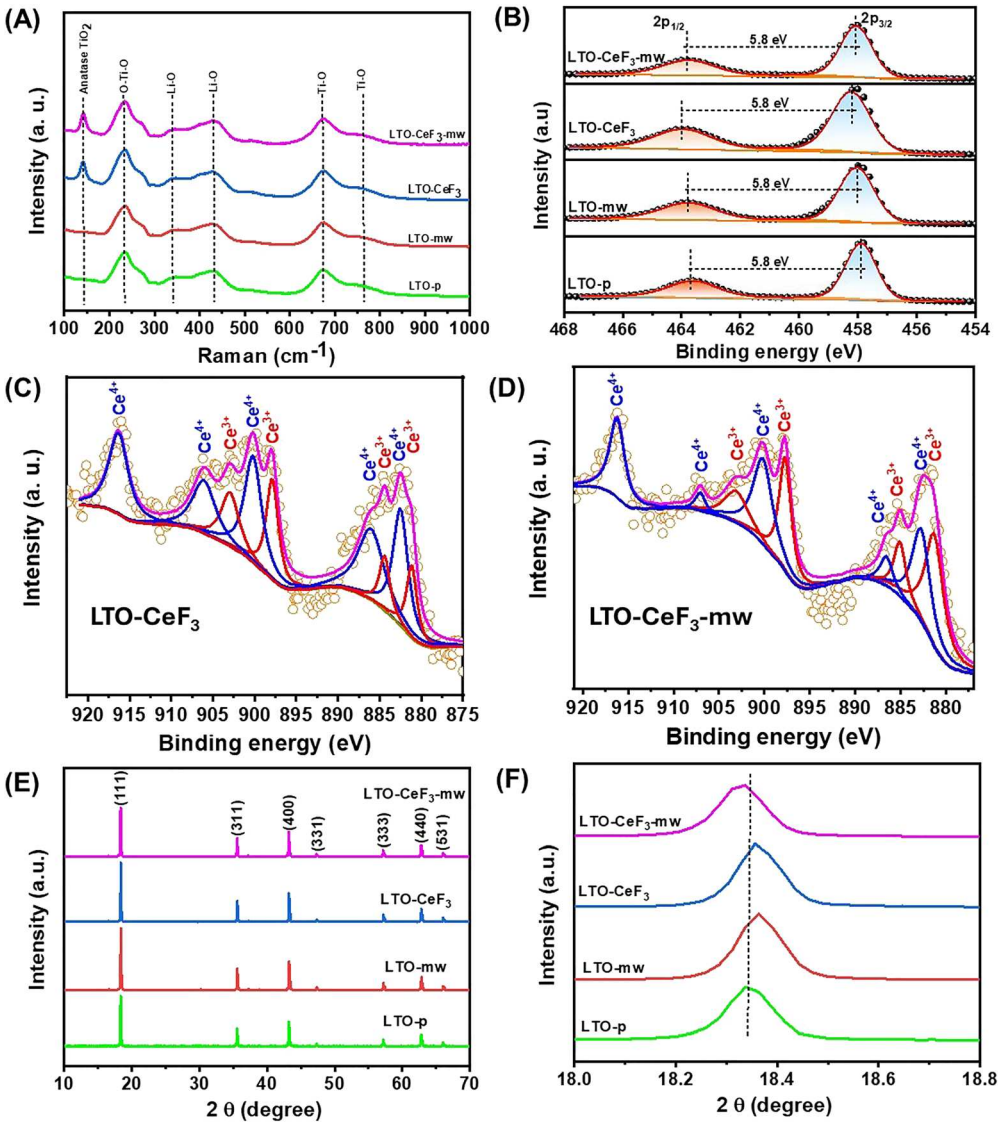

Fig. 4 (A) Raman spectra of LTO-p, LTO–mw, LTO–CeF_3 and LTO–CeF_3–mw; (B) XPS, Ti 2p of LTO-p, LTO–mw, LTO–CeF_3 and LTO–CeF_3–mw; (C) XPS, Ce 3d of LTO–CeF_3; (D) XPS, Ce 3d of LTO–CeF_3–mw; (E) XRD patterns of the LTO-p, LTO–mw, LTO–CeF_3 and LTO–CeF_3–mw; (F) XRD patterns of the lattice plane (111) of LTO-p, LTO–mw, LTO–CeF_3 and LTO–CeF_3–mw.

Second, in LTO–mw, the peak (111) shifted to the higher 2θ degree position relative to that of the LTO-p. Again, this indicates that there is lattice contraction in the microwave-irradiated sample LTO–mw. The shift to the higher angle may have resulted from the microwave irradiation-induced lattice distortion, as shown in the HRTEM image (Fig. 3A, region I). Nozariasbmarz *et al.*[49] proposed that the fast heating and high electric field of microwave irradiation can distort the atoms from their lattice sites and thus cause lattice strain[28] which resulted in the shift to the higher 2θ degree position. The lattice contraction is corroborated by the HRTEM lattice *d*-spacing.

Third, in LTO–CeF_3–mw, the peak (111) shifted to the lower 2θ degree position relative to the LTO-p. This indicates that there is lattice expansion in the LTO–CeF_3–mw. It is interesting to note that unlike the microwave sample (LTO–mw) and non-microwave-irradiated coated sample (LTO–CeF_3) that show lattice contraction, the microwave-irradiated coated sample (LTO–CeF_3–mw) shows lattice expansion. The lattice expansion of the microwave-irradiated coated sample is caused by the synergetic effect of the presence of point defects and electromagnetic irradiation. Though the coated sample LTO–CeF_3 has point defects but experienced lattice contraction, this may be because of the absence of microwave irradiation. Furthermore, the microwave sample LTO–mw also experienced lattice contraction because of the absence of the point defects. Hence, the lattice expansion occurs when there is a combined use of point defects and microwave irradiation. Yu *et al.*[50] reported that point defects are better microwave absorbers. Thus, it can be proposed that the point defects in LTO–CeF_3–mw sample enabled better microwave absorption and thus caused its lattice expansion relative to the lattice contraction in LTO–mw that has no point defects. It may therefore be concluded that the

lattice expansion in the LTO–CeF_3–mw sample resulted from the microwave irradiation *via* the point defects. Hence, it is expected that LTO–CeF_3–mw electrode material will have the smoothest Li^+ diffusion. These results are also in agreement with the calculated lattice constants of the four samples using the Bragg's law ($n\lambda = 2d\sin\theta$). Table S1 shows the calculated lattice constants of the LTO samples using the 2θ degree position of the most intense peak (111). The calculated lattice constants for LTO-p, LTO–mw, LTO–CeF_3 and LTO–CeF_3–mw are 8.3699, 8.3609, 8.3635 and 8.3762 Å, respectively. These results are comparable with the literature reports.[51,52] The lattice constants of the LTO–mw (8.3609 Å) and LTO–CeF_3 (8.3635 Å) are less than that of the LTO-p (8.3699 Å), which confirms the lattice contraction as evidenced in Fig. 4F by the shift of the LTO–mw and LTO–CeF_3 peaks (111) to the higher 2θ degree position relative to that of LTO-p. The lattice constant of the LTO–CeF_3–mw (8.3762 Å) is more than that of the LTO-p (8.3699 Å), which confirms the lattice expansion as evidenced in Fig. 4F by the shift of the LTO–CeF_3–mw peak (111) to the lower 2θ degree position relative to that of LTO-p.

The adsorption isotherms (Fig. S3) of all the samples show a type III profile. The BET parameters for the LTO samples are presented in Table S2. Nitrogen gas adsorption results reveal that the surface area of LTO-p, LTO–mw, LTO–CeF_3 and LTO–CeF_3–mw are 4.18, 2.29, 3.89 and 5.28 ($m^2\ g^{-1}$), respectively. The microwave-irradiated coated sample LTO–CeF_3–mw has the largest BET surface area compared with the surface-coated LTO–CeF_3 sample and microwave-irradiated sample LTO–mw. LTO–CeF_3–mw has a higher surface area than LTO–mw because the LTO–CeF_3–mw sample has defects that enhanced the absorption of microwave irradiation, allowing it to absorb more energy (heat), which resulted in smaller particle sizes and, hence, a higher surface area than the other 3 samples. Consequently, the LTO–CeF_3–mw electrode has the largest surface area and it is expected to have more Li^+ insertion sites and effective electrolyte contact for faster Li^+ kinetics.

3.1 Electrochemical measurements

3.1.1 Cyclic voltammetry (CV). Fig. 5A shows the CV curves of the LTO-p, LTO–mw, LTO–CeF_3 and LTO–CeF_3–mw electrodes at 0.1 mV s^{-1} scan rate between the voltage window of 1.0 and 2.5 V (*vs.* Li/Li^+). The redox peaks around 1.55 V and 1.6 V in the CV curves of all the samples are the Li^+ intercalation/deintercalation in the spinel LTO (eqn (2)).

$$Li_4Ti_5O_{12} + 3Li^+ + 3e^- \rightarrow Li_7Ti_5O_{12} \quad (2)$$

The redox peaks of the coated electrode materials LTO–CeF_3 and LTO–CeF_3–mw are narrower (Fig. 5B) and have higher current responses than those of the uncoated electrode materials LTO-p and LTO–mw (Fig. 5A). These narrower redox peaks indicate the fast kinetics and remarkable efficiency of the insertion/extraction process of Li^+ in the spinel lattice, which may be attributed to the presence of point defects in these two

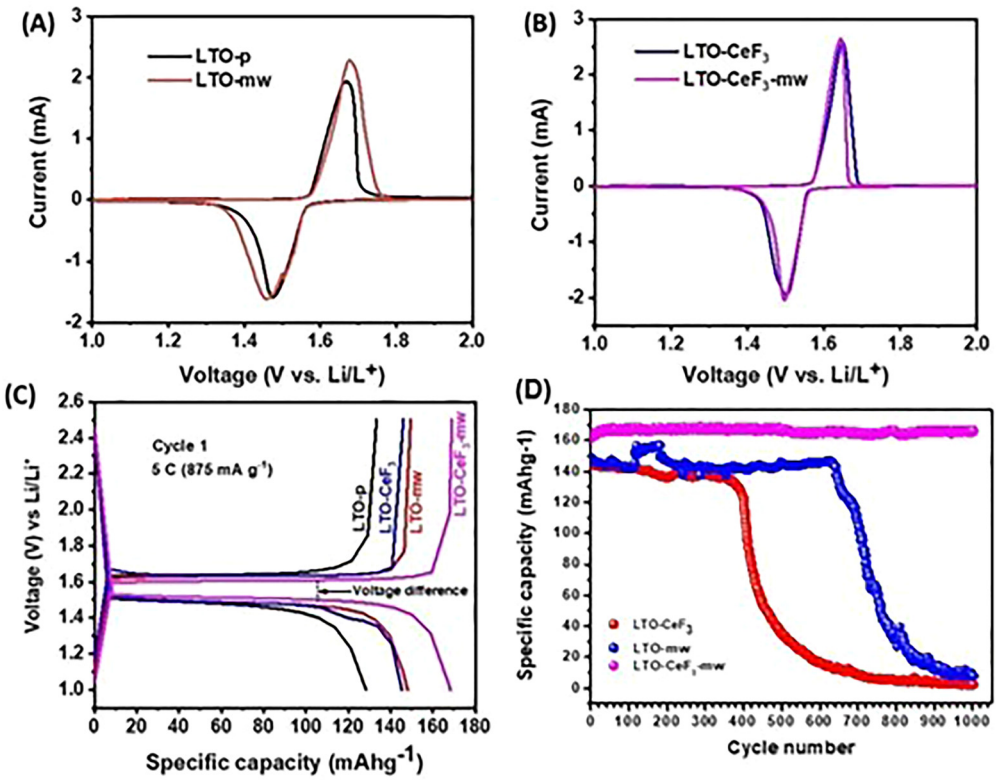

Fig. 5 (A) CV at 0.1 mV s^{-1} of (A) LTO-p and LTO–mw, (B) LTO–CeF_3 and LTO–CeF_3–mw, (C) GCD cycle 1 of LTO-p, LTO–CeF_3, LTO–mw, and LTO–CeF_3–mw (D) specific capacity *vs.* cycle number at 5C of LTO–CeF_3, LTO–mw and LTO–CeF_3–mw.

samples. Furthermore, the CV for the coated samples did not show additional redox peaks around 1.70/2.05 V for the Li^+ insertion/extraction within the anatase TiO_2 lattices, unlike some previous reports.[4,53,54] This suggests a very weak electrochemical activity of TiO_2 because of the low amount of TiO_2 in these coated LTO samples.

Table 2 shows (i) the peak-to-peak separation voltage (E_{pp}/V), which indicates the electron transfer kinetics electrode materials; (ii) the peak heights of the anodic (I_{pa}/mA) and cathodic (I_{pc}/mA) curves, which confirm the mass transport and redox dynamics, and (iii) the ratio of the peak current (I_{pa}/I_{pc}), which shows the reversibility. The coated electrode materials LTO–CeF_3 and LTO–CeF_3–mw have the lowest E_{pp} of 0.15 V compared with the uncoated materials LTO (0.20 V) and LTO–m (0.22 V). This means that the CeF_3 coating improves the electron transfer kinetics of LTO compared to uncoated LTO materials. This electrochemical improvement may be attributed to the presence of point defects in these two samples. These results show that microwave irradiation does not affect the electron transfer kinetics of the materials. Furthermore, the point defects improve the mass transport in the coated materials as shown by the higher current response of the coated materials. However, the microwave-irradiated coated (LTO–CeF_3–mw) electrode has the highest values of I_{pa} and I_{pc} (mass transport) because of the synergic effect of the CeF_3 coating and microwave irradiation that led to better CeF_3 surface coat, as established by HRTEM above (Fig. 2D). Despite this, the I_{pa}/I_{pc} ratio suggests that neither the microwave treatment nor the point defects significantly affect the reversibility of the redox processes (*i.e.*, Coulombic efficiency). Nevertheless, the LTO–mw shows a larger/broader profile which signifies larger Li^+ storage. Furthermore, the CV is used to quantify the surface capacitance of (220) and (310) planes by the empirical power-law relationship between peak current and scan rate in the cyclic voltammograms (CVs) of the LTO-p, LTO–mw, LTO–CeF_3 and LTO–CeF_3–mw at 0.1, 0.3, 0.5 and 1.0 mV s^{-1} (Fig. S5). Therefore, using power-law equation:

$$i = av^b \tag{3}$$

eqn (3) can be written in the logarithmic form:

$$\mathrm{Log}\, i = b \log v + \log a \tag{4}$$

where i is the peak current, v is the scan rate, b and a are the slope and intercept, respectively. Generally, the value of b is normally between 0.5 and 1. When the value of b is close to 1, it suggests capacitive contribution, that is, the mechanism is *via* surface charge storage (non-faradaic). This surface charge storage mechanism involves the accumulation of charge at the electrode–electrolyte interface. When the value of b is close to 0.5, it suggests that the mechanism is *via* diffusion control (faradaic process). That is, the current is limited by the kinetics of the redox process. The plots of $\log(i)$ *vs.* $\log(v)$ for the four samples are shown in Fig. S6. Fig. S6 and Table S3 show that the value of b for all the samples is approximately 0.5. The b value indicates that the charge storage mechanism for all the four samples is faradaic. However, the faradaic charge storage mechanism can further be classified as diffusion-controlled or non-diffusion-controlled (pseudocapacitive). The pseudocapacitive mechanism relates to the surface capacitive non-faradaic (capacitive contribution).[55] Therefore, to calculate the quantitative capacitive contribution, the power-law eqn (3) may be classified into Faraday current (diffusion-controlled) and surface capacitive non-Faraday (non-diffusion-controlled) currents and the total current at a fixed voltage is

$$i\,(V) = k_1 v + k_2 v^{1/2} \tag{5}$$

where i = total current response at a fixed voltage V and is calculated as the sum of the non-diffusion-controlled ($k_1 v$) and the diffusion-controlled ($k_2 v^{1/2}$) currents.

Rearranging eqn (5)

$$i\,(V)/v^{1/2} = k_1 v^{1/2} + k_2 \tag{6}$$

Hence, the values of k_1 and k_2 may be used to separate the fraction of the current result from diffusion-controlled and non-diffusion-controlled, respectively, at fixed voltages. Therefore, Fig. S7 shows that the CV at 0.1 mV m^{-2} of LTO–mw has 35% surface capacitance (non-diffusion-controlled), while LTO–CeF_3–mw has 28%. It may thus be proposed that the surface capacitance of the surface lattice planes (220) and (310) of the LTO–mw (35%) is greater than that of LTO–CeF_3–mw (28%).

3.1.2 Galvanostatic charge–discharge (GCD). One of the key challenges of LTO as an anode material for LIBs is the poor capacity at a high rate that limits its large-scale applications in energy storage. Therefore, this study commenced its investigation by carrying out the GCD measurement on the four anode materials at a high rate of 875 mA g^{-1} (5C) between a voltage window of 1.0 and 2.5 V (*vs.* Li/Li^+). Fig. 5C shows the discharge–charge voltage profiles for the first cycle at a current density of 5C for the four samples. All four samples show a flat discharge plateau at around 1.55 V, which is the characteristic of the extraction of Li^+ from the spinel LTO. This is consistent with the CV result. The first cycle discharge capacity at 5C of the LTO-p, LTO–mw, LTO–CeF_3 and LTO–CeF_3–mw anodes are 128.3, 148.1, 145.4 and 168.3 mAh g^{-1}, respectively. The higher specific capacity of LTO–CeF_3 (145.4 mAh g^{-1}) than that of LTO-p (128.3 mAh g^{-1}) can be suggested to relate to the presence of the point defects in its lattice structure. This is because the TiO_2 redox peaks/plateau around 1.70/2.05 V are absent in the cyclic voltammogram and GCD profile; hence, TiO_2 is not responsible for the increased capacity, but the point defects. This finding differs from previous reports where the presence of TiO_2 caused the increased capacity.[4,56] Thus, it can be concluded that the defects in the coated sample LTO–CeF_3 caused the enhanced conductivity compared to the defect-free

Table 2 CV redox reaction parameters for the samples

Electrode	E_{pa}/V	E_{pc}/V	ΔE/V	I_{pa}/mA	I_{pc}/mA	I_{pa}/I_{pc}
LTO-p	1.67	1.47	0.20	1.91	1.57	1.22
LTO–mw	1.68	1.46	0.22	2.28	1.58	1.44
LTO–CeF_3	1.65	1.50	0.15	2.53	1.94	1.30
LTO–CeF_3–mw	1.65	1.50	0.15	2.59	1.98	1.31

pristine sample LTO-p. These findings, and the non-obvious presence of TiO_2 in the XRD patterns, show that the amount of TiO_2 may be very small to cause obvious effects on the electrochemical properties of the coated samples. The higher specific capacity of LTO–mw (148.1 mAh g^{-1}) may be related to the microwave irradiation's introduction of new lattice planes LTO (220), (222) and (310) into its lattice structure. It may be suggested that microwave irradiation tuned the lattice plane (111) in LTO-p to (220), (222) and (310) in the LTO–mw. It is common knowledge that the electrode materials' surface properties have a significant effect on their electrochemical performance. Therefore, the surface lattice plane (220), (222) and (310) in LTO–mw exposed larger number of surface sites that allow more Li^+ storage (as shown by the larger CV peak area in Fig. 5A) that led to the higher specific capacity of 148.1 mAh g^{-1} at 5C. The LTO–CeF_3–mw anode material has the highest specific capacity of 168.3 mAh g^{-1} and the smallest voltage difference between the charge and discharge profiles which suggests weak polarization as shown in Fig. 5C. These findings are consistent with the CV results. Furthermore, electrochemical analysis is thus focused on the modified sample (LTO–mw, LTO–CeF_3 and LTO–CeF_3–mw) materials, since the pristine sample (LTO) has the lowest performance in terms of specific capacity.

Therefore, the long cyclic stability performance of LTO–mw, LTO–CeF_3 and LTO–CeF_3–mw electrode materials was carried out at 875 mA g^{-1} (5C) for 1000 cycles (Fig. 5D). The percentage capacity retention, which is used to assess the cyclic stability, can be calculated from *n*th cycle (final cycle) discharge capacity divided by the initial discharge capacity multiply by 100. LTO–CeF_3–mw delivers the highest initial specific capacity of 168 mA h g^{-1} and has a high capacity retention of 98.9% (166.1 mA h g^{-1}) after 1000 cycles. While LTO–mw and LTO–CeF_3 cells have initial capacities of 148.1 and 145.4 mA h g^{-1} and capacity retentions of 5.2% (7.7 mA h g^{-1}) and 1.8% (2.6 mA h g^{-1}), respectively, after 1000 cycles. The LTO-mw electrode exhibits poor capacity retention due to its exposed, uncoated surface, which is susceptible to electrolyte attack. The LTO–CeF_3 shows lower specific capacity and poor capacity retention because it has only the surface lattice plane (111). Wei[57] emphasized the significance of surface orientation to the electrochemical performance of spinel electrode materials and reported similar poor electrochemical performance for the exposed crystal plane (111). The LTO–CeF_3–mw has the highest capacity retention of 98.9% because of its higher surface area and increased lattice spacing. It is very important to note this remarkable property of LTO–CeF_3–mw in exhibiting significantly low capacity fading during the long-term charge–discharge cycles. Also, Fig. S4 shows that the LTO–CeF_3–mw electrode has an outstanding Coulombic efficiency of ~100%. In addition, the LTO–CeF_3–mw electrode has an outstanding Coulombic efficiency of ~100% for both the 1st and the 1000th cycles. In contrast, LTO–mw has Coulombic efficiency of ~101% for the 1st and 113% for the 1000th cycle, and LTO–CeF_3 has ~100% Coulombic efficiency for the 1st cycle and 93% for the 1000th cycle. These remarkable performances of LTO–CeF_3–mw electrode material could be attributed to the lattice expansion, large surface that has more active sites for Li^+ storage and enhanced the effective electrolyte contact for faster Li^+ kinetics.

Fig. 6A shows the capacity-rate performances of the LTO–mw, LTO–CeF_3 and LTO–CeF_3–mw cells at different current densities of 87.5 mA g^{-1} (0.5C), 175 mA g^{-1} (1C), 525 mA g^{-1} (3C), 1750 mA g^{-1} (10C) and 87.5 mA g^{-1} (0.5C). The two microwave-irradiated samples show the highest discharge capacities from 0.5C to 10C. This performance could be attributed to the presence of the newly tuned surface lattice planes LTO (220) and (330) introduced by microwave irradiation. The microwave-irradiated non-coated sample LTO–mw has a specific capacity of 196.6, 192.5 and 120.9 mAh g^{-1} at 87.5 mA g^{-1} (0.5C), 175 mA g^{-1} (1C), 1750 mA g^{-1} (10C), respectively, and the microwave-irradiated coated sample LTO–CeF_3–mw has specific capacities of 195.2, 191.1 and 119.9 mAh g^{-1}, respectively. This slightly improved performance of LTO–mw, despite its lower BET surface area, may be related to it having more exposed surface lattice planes (220), (222) and (310) than the sample LTO–CeF_3–mw that has only (220) and (310). The surface lattice plane is distinctly different from the BET surface area. The surface lattice plane relates to the geometrical arrangement of atoms in the crystal structure, and their orientation is identified by Miller indices. The orientation is of great importance as it affects the crystal's properties such as surface reactivity. While the BET surface area is the total accessible area and is usually measured by the amount of nitrogen gas physically absorbed at a specific temperature and pressure. At the high charge-rate (C-rate) of 1750 mA g^{-1} (10C), the LTO–CeF_3, LTO–mw and LTO–CeF_3–mw have specific capacities of 99.9, 120.9 and 119.9 mAh g^{-1}, respectively. The uncoated microwave-irradiated sample LTO–mw has a higher specific capacity (120.9 mAh g^{-1}) than the coated sample LTO–CeF_3 (99.9 mAh g^{-1}). This confirms that the CeF_3 surface modification (TiO_2 and point defects) is not the cause of the increase in specific capacities of the LTO–mw and LTO–CeF_3–mw electrode materials, but because of the tuned surface lattice planes (220), (222) and (310). This finding suggests that the LTO surface lattice planes (220), (222) and (310) are more electrochemically active sites than the lattice plane (111).

It is of interest to note that Fig. 6A shows that the microwave-irradiated samples LTO–mw, and LTO–CeF_3–mw have high specific capacities of 192.5 and 191.1 mAh g^{-1} at 1C which are greater than the theoretical specific capacity of LTO (175 mAh g^{-1}) in the voltage window of 2.5 to 1.0 V.

These higher values, greater than the theoretical specific capacity of 175 mAh g^{-1} at 1C for LTO specific capacity, are consistent with previous reports, but most of these reports are in the voltage window of 2.5 to 0.01 V[58,59] or have dual-phase $Li_4Ti_5O_{12}$–TiO_2 composites.[4,56]

$$\mathbf{Li_{3(8a)}[LiTi_5^{4+}]_{(16d)}O_{12(32e)} \xleftrightarrow{+3e^- / +3Li^+} Li_{6(16c)}[LiTi_3^{3+}Ti_2^{4+}]_{(16d)}O_{12(32e)}} \quad (7)$$

Conventionally, it is thought that the specific capacity of LTO is limited by the number of octahedral sites (16d) that can accommodate Li (*i.e.* $C_{th} \approx 175$ mAh g^{-1}; eqn (7)).

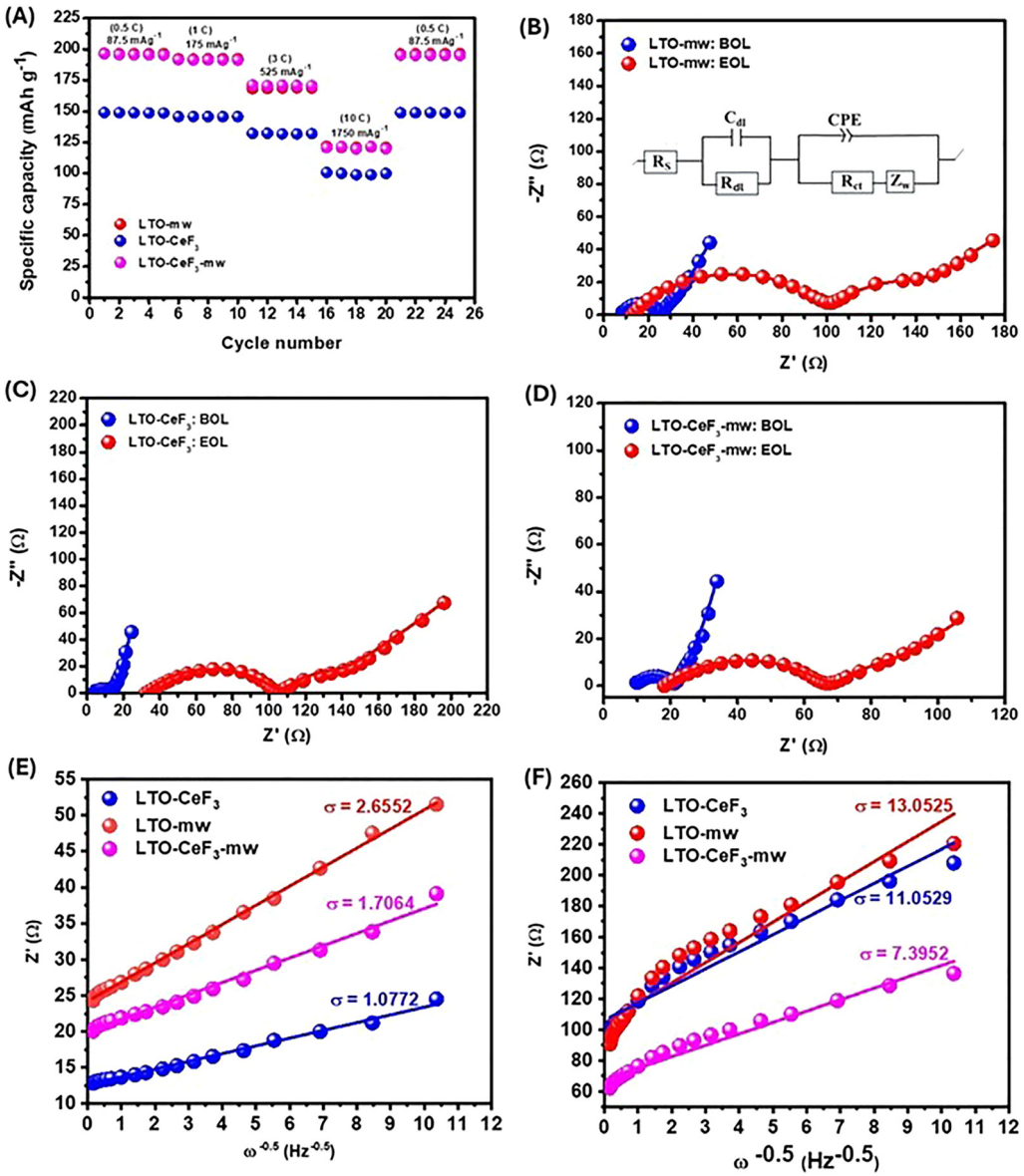

Fig. 6 (A) Rate capability of LTO–CeF_3, LTO–mw, and LTO–CeF_3–mw; electrochemical equivalent impedance before cycling and after 1000 cycles of (B) LTO–mw (inset is the electrochemical equivalent circuit used for the samples), (C) LTO–CeF_3 and (D) LTO–CeF_3–mw. (E) Plot of Z' *vs.* $\omega^{-1/2}$ BOL and (F) plot of Z' *vs.* $\omega^{-1/2}$ EOL.

However, it has been recognized that the tetrahedral sites (8a) can accommodate extra Li (considering that 16c is fully occupied) from the available number of tetravalent Ti (the 2 moles of Ti^{4+} in the octahedral site (16d) in eqn (3)) (*i.e.*, $C_{th} \approx$ 292 mAh g^{-1}; eqn (8)).

$$Li_{6(16c)}[Ti_3^{3+}Ti_2^{4+}]_{(16d)}O_{12(32e)} \xleftrightarrow{+2e^- / +2Li^+} Li_{2(8a)}Li_{6(16c)}[LiTi_5^{3+}]_{(16d)}O_{12(32e)} \quad (8)$$

But it should perhaps not be surprising that the tetrahedral sites (8a) may simply accommodate just an extra 0.5 mole of Li instead of 2 moles of Li from the available 2 moles of Ti^{4+} as observed in our study: microwave treatment (*i.e.*, $C_{th} \approx$ 204 mAh g^{-1}; eqn (9)).

$$Li_{6(16c)}[Ti_3^{3+}Ti_2^{4+}]_{(16d)}O_{12(32e)} \xleftrightarrow{+0.5e^- / +0.5Li^+} Li_{0.5(8a)}Li_{6(16c)}[LiTi_{3.5}^{3+}Ti_{1.5}^{4+}]_{(16d)}O_{12(32e)} \quad (9)$$

This study is different in that the voltage window used for all the electrochemical measurements is 2.5 to 1.0 V and the LTO–mw anode material that has the highest capacity of 192.5 mAh g^{-1} at 175 mA g^{-1} (1C) does not have the dual phase. It is important to note that though LTO–mw has the highest specific capacity at 1C, Fig. 6A and Table 2 show that the conventional limiting factors (Li^+ diffusion, Li^+ transport and electron transport) are not applicable nor responsible for the high capacity. This is because the LTO–mw has the highest CV peak-to-peak separation voltage (E_{pp}/V), which signifies the

highest polarization effect that translates to low kinetics. Amazingly, this is the electrode material that has the highest specific capacity of all the samples and has a specific capacity higher than the theoretical specific capacity. Consequently, this outstanding performance may be related to the LTO–mw having large Li^+ storage as shown in the CV profile area. This agrees with the LTO–mw's CV analysis above and Fig. S7 that show its surface capacitance has a non-faradaic (non-diffusion) process of 35% which is greater than that of the LTO–CeF_3–mw (28%). This confirms that the surface capacitive of the non-diffusion process' specific capacity share of LTO–mw is greater than that of LTO–CeF_3–mw. This may suggest the reason why the LTO–mw has the highest specific capacity of 192.5 mAh g^{-1} at 175 mA g^{-1} (1C) relative to the other samples. Cunha *et al.*[60] have attributed similar higher specific capacity than the theoretical capacity within the voltage window of 2.5 to 1.0 V to a surface-related phenomenon, where the surface of the spinel LTO having different surface lattice planes played a significant role in the Li^+ storage properties. That is, the higher specific capacity than the theoretical capacity of LTO within the voltage window of 2.5 to 1.0 V is due to significant surface contributions in Li^+ storage. Hence, this higher discharge capacity of LTO–mw can be suggested to be because of the surface lattice planes (220), (222) and (310) having significant contributions in lithium storage.

On the other hand, it is also pertinent to point out that the LTO–CeF_3–mw sample has a specific capacity of 191.1 mAh g^{-1} at 175 mA g^{-1} (1C) within the voltage window of 2.5 to 1.0 V. This is higher than the theoretical specific capacity. Even though the Raman and HRTEM show the presence of TiO_2 in the LTO–CeF_3–mw, it can be suggested that the TiO_2 is not responsible for the higher specific capacity, as evident by the absence of the CV redox peaks and GCD voltage plateau at 1.70 V/2.08 V that are synonymous with TiO_2 contribution to specific capacity.[4] This also confirms that the higher discharge capacity may have resulted from Li^+ storage at the surface lattice planes (220) and (310). It is impressive to emphasize that all three samples recover to their initial discharge capacities when the rate returns to 87.5 mA g^{-1} (0.5C). This shows the good reversibility of the modified LTO samples. Furthermore, the performance characteristics (rate capability and cycling performance) of the LTO–CeF_3–mw anode material surpass most of the summarized reports categorized as ''high performance'' by Kazemi *et al.*[61]

3.1.3 Electrochemical impedance spectroscopy (EIS). Fig. 6(B)–(D) shows the Nyquist plots of LTO–mw, LTO–CeF_3 and LTO–CeF_3–mw samples before and after cycling. Before cycling, all the materials have one high- to medium-frequency semicircle and one low-frequency sloped line. After cycling, two partially overlapped and depressed semicircles are observed in the high- to medium-frequency regions for LTO–mw, and LTO–CeF_3. The EIS parameters are made up of the solution resistance (R_s) attributed to the electrolyte's ohmic resistance and the charge-transfer resistance (R_{ct}) at the intermediate frequency regions corresponding to the redox processes, which highlight the exchange of Li^+ ions at the surface of the electrode. The C_{dl} indicates the double-layer capacitances, and Warburg impedance (Z_W) offers insights on the impedance of Li^+ ion diffusion in bulk electrode materials. The R_{dl} signifies the high-frequency resistance due to the double layer, while the constant phase element (CPE) is the interfacial capacitance.[62] Table S4 shows values for the EIS parameters before cycling: beginning-of-life (BOL), while Table S5 shows the parameters after 1000 cycles: end-of-life (EOL). Table S4 shows that the LTO–CeF_3 has the lowest R_{ct} (7.07 Ω) while LTO–CeF_3–mw has a higher R_{ct} (9.38 Ω) and LTO–mw has the highest R_{ct} (15.15 Ω). The LTO–mw has the highest charge transfer resistance, which agrees with the CV (E_{pp}/V) that signifies the highest polarization effect (low kinetics). However, the LTO–mw electrode material has the highest specific capacity at 1C. Therefore, the EIS confirms that the specific capacity of the microwave irradiated electrode–LTO–mw does not relate to the kinetics, but to the surface plane orientation's contribution to large Li^+ storage as shown in the CV profile area (Fig. S5 and the surface capacitive non-diffusion process (Fig. S7A and B). The same reason accounts for why the coated microwave-irradiated electrode LTO–CeF_3–mw has a higher specific capacity than the non-microwave-irradiated electrode LTO–CeF_3. It may therefore be attributed to the surface lattice plane phenomenon caused by microwave irradiation, as against the conventional enhanced specific capacity that resulted from enhanced kinetics. The same explanation goes for the Z_W values 2.79, 4.25 and 6.88 Ω, respectively, for LTO–CeF_3, LTO–CeF_3–mw and LTO–mw before GCD (BOL). Table S5 shows the EOL EIS parameters of the three battery chemistries. The results show that LTO–CeF_3–mw has less impedance relative to LTO–mw and LTO–CeF_3. The microwave sample LTO–mw has the highest values of 24.28, 91.1 and 26.65 Ω for R_{SEI}, R_{ct} and Z_{tw}, respectively, while the coated microwave sample LTO–CeF_3–mw has the lowest values of 6.68, 53.39 and 17.72 Ω, respectively. To further investigate the electrochemical performance of these three samples, the Li^+ diffusion kinetics of the electrodes were calculated from eqn (10).

$$D_{Li^+} = \frac{2(RT)^2}{(An^2F^2C_{Li^+})} \quad (10)$$

where D_{Li^+} is the Li^+ diffusion coefficient (rate of Li^+ transport), R is the gas constant, T is the absolute temperature, A is the surface area of the electrode, n is the number of electrons per molecule during oxidation, F is the Faraday's constant, C_{Li^+} is Li^+ concentration and σ is the Warburg factor. The Warburg factor, σ, is the slope of the plot of Z' *vs.* $\omega^{-1/2}$ shown in Fig. 6E and F and in the eqn (11).

$$Z' = R_s + R_{ct} + \sigma\omega^{-1/2} \quad (11)$$

where Z' is the impedance obtained from the lower frequency regions plots of Fig. 6B–D, and ω is the angular frequency. Fig. 6E and F show a linear relationship and the values of the slopes (σ) which are presented in Tables S4 and S5. The D_{Li^+} is a measure of how fast Li^+ diffuses and is thus calculated by substituting σ in eqn (11), and the calculated D_{Li^+} values are presented in Tables S4 and S5. Table S4 (EIS-BOL) results show

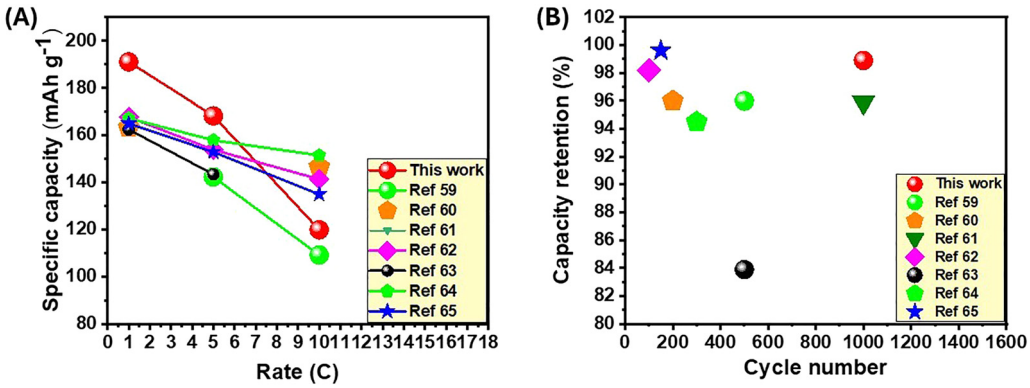

Fig. 7 (A) Comparison of rate capacities of LTO–CeF_3–mw anode material in this work with LTO anode materials previously reported. (B) Comparison of capacity retention at 875 mA g^{-1} (5C) of LTO–CeF_3–mw anode material in this work with LTO anode materials previously reported.

that LTO–CeF_3 has the highest diffusion coefficient of 4.2×10^{-8} cm^2 s^{-1} followed by LTO–CeF_3–mw (1.7×10^{-8} cm^2 s^{-1}) and LTO–mw has least (6.9×10^{-8} cm^2 s^{-1}). These results are also in agreement with those of the CV. The Li^+ diffusion coefficient results also confirm that the enhanced specific capacity of the microwave sample (LTO–mw) is not a function of the Li^+ kinetics. It may therefore be proposed that the enhanced specific capacity of the LTO–mw electrode is because of the change in the surface lattice plane. However, Table S5 (EIS-EOL) results show that LTO–CeF_3–mw has the highest diffusion coefficient of 8.8×10^{-10} cm^2 s^{-1} followed by LTO–CeF_3 (4.0×10^{-10} cm^2 s^{-1}) and LTO–mw has least (6.9×10^{-10} cm^2 s^{-1}). The Li^+ diffusion coefficient result of LTO–CeF_3–mw confirms that the enhanced electrochemical performances of the coated microwave-irradiated sample are not only a function of the Li^+ kinetics caused by CeF_3-coated surface but are also functions of the introduced surface lattice planes, lattice expansion, and increased BET surface area caused by the synergy between the coated surface and microwave irradiation.

Fig. 7A shows the comparison of rate capacities of LTO–CeF_3–mw anode material in this work with LTO anode materials previously reported, while Fig. 7B shows the comparison of capacity retention at 875 mA g^{-1} (5C) of LTO–CeF_3–mw anode material in this work with LTO anode materials.[63–69] The compared parameters show that relative to these previous studies, the electrochemical performance of microwave-coated sample, LTO–CeF_3–mw, is remarkable.

4. Conclusion

This research work strategically used microwave irradiation and CeF_3 surface coating to synthesize the LTO–CeF_3–mw anode material for LIBs that has an outstanding specific capacity of 191.1 mAh g^{-1} at 175 mA g^{-1} (1C) which is greater than the theoretical specific capacity of LTO (175 mAh g^{-1}). Furthermore, the LTO–CeF_3–mw electrode has long-term cycling stability with high-capacity retention of 98.9% after 1000 cycles, high-rate of specific capacity of 119.9 mAh g^{-1} at 10C and reversible capacity. These top-notch electrochemical performances of the LTO–CeF_3–mw can be attributed to the tuned surface lattice planes (220) and (310) from (111), expanded lattice spacing and high surface area. The findings of this study are of great importance to the advancement towards high-energy, high-power and long-life LIBs for electric vehicles' large-scale energy storage.

Conflicts of interest

There are no conflicts to declare.

Data availability

The data supporting this article have been included as part of the supplementary information (SI). The supplementary information includes additional data supporting this study. Fig. S1 presents SEM–EDS elemental mapping of all four samples: (A) LTO-p, (B) LTO–mw, (C) LTO–CeF_3, and (D) LTO–CeF_3–mw. Fig. S2 shows HRTEM micrographs of LTO-p. Table S1 exhibits the lattice constants of the four samples. Fig. S3 provides N_2 adsorption/desorption isotherms, while Table S2 lists the corresponding BET surface area and porosity parameters. Fig. S4 displays galvanostatic charge–discharge profiles for cycle 1 and cycle 1000 at 5C for (A) LTO–CeF_3, (B) LTO–mw, and (C) LTO–CeF_3–mw. Fig. S5 presents cyclic voltammograms recorded at scan rates of 0.1, 0.3, 0.5, and 1.0 mV s^{-1} for all samples, and Fig. S6 shows the corresponding log (peak current) *versus* log (scan rate) plots. Table S3 reports the calculated *b*-values at different scan rates. Fig. S7 compares the capacitive and diffusion-controlled contribution fractions for (A, B) LTO–mw and (C, D) LTO–CeF_3–mw. Tables S4 and S5 show the electrochemical impedance spectroscopy (EIS) fitting parameters before cycling (BOL) and after 1000 cycles (EOL), respectively. See DOI: https://doi.org/10.1039/d5ya00303b.

Acknowledgements

The authors are grateful for the financial support from the following: (i) UCL-Wits collaboration Seed Fund, (ii) Fellowship of the Association of the Commonwealth Universities (ACU) for

partnership with the Coventry University (UK), and (iii) the DSI-NRF-Wits SARChI Chair in Materials Electrochemistry and Energy Technologies (MEET) (UID No.: 132739). JJH acknowledges funding from EPSRC (EP/T517793/1).

References

1 B. Yan, M. Li, X. Li, Z. Bai, J. Yang, D. Xiong and D. Li, Novel understanding of carbothermal reduction enhancing electronic and ionic conductivity of $Li_4Ti_5O_{12}$ anode, *J. Mater. Chem. A*, 2015, **3**, 11773–11781.

2 A. Yu, D. Gong, M. Zhang and Y. Tang, In-situ implanted carbon nanofilms into lithium titanate with 3D porous structure as fast kinetics anode for high-performance dual-ion battery, *Chem. Eng. J.*, 2020, **401**, 125834.

3 Y.-J. Bai, C. Gong, N. Lun and Y.-X. Qi, Yttrium-modified $Li_4Ti_5O_{12}$ as an effective anode material for lithium ion batteries with outstanding long-term cyclability and rate capabilities, *J. Mater. Chem. A*, 2013, **1**, 89–96.

4 M. Akhtar, T. Majumder, J.-K. Chang and S. B. Majumder, High-Performance and Safe Hybrid Li-Ion Batteries Based on $Li_4Ti_5O_{12}$ –TiO_2 (A)–TiO_2 (R)@C Anode and $Na_3V_2O_2(PO_4)_2F$–$Na_3V_2(PO_4)_3$@C Cathode, *ACS Sustainable Chem. Eng.*, 2022, **10**, 1390–1397.

5 C. Ho, C. V. Li, K. Chan, H. Yung and Y. Tay, Interfacing TiO_2 (B) Nanofibers with $Li_4Ti_5O_{12}$ Towards Highly Reversible and Durable TiO_2 -based Anode for Li−Ion Batteries, *Energy Technol.*, 2019, **7**, 107–112.

6 H. Chang, Y.-R. Wu, X. Han and T.-F. Yi, Recent developments in advanced anode materials for lithium-ion batteries, *Energy Mater.*, 2022, **1**, 100003.

7 X. Bai, T. Li and Y.-J. Bai, Capacity degradation of $Li_4Ti_5O_{12}$ during long-term cycling in terms of composition and structure, *Dalton Trans.*, 2020, **49**, 10003–10010.

8 A. Lakshmi-Narayana, M. Dhananjaya, C. M. Julien, S. W. Joo and C. V. Ramana, Enhanced Electrochemical Performance of Rare-Earth Metal-Ion-Doped Nanocrystalline $Li_4Ti_5O_{12}$ Electrodes in High-Power Li-Ion Batteries, *ACS Appl. Mater. Interfaces*, 2023, **15**, 20925–20945.

9 Z. Wang, H. Guo, D. Ning, X. Ma, L. Zheng, D. Smirnov, K. Sun, D. Chen, L. Sun and X. Liu, Tuning Fermi level and band gap in $Li_4Ti_5O_{12}$ by doping and vacancy for ultrafast Li^+ insertion/extraction, *J. Am. Ceram. Soc.*, 2021, **104**, 5934–5945.

10 A. Sohib, S. Priyono, W. B. Widayatno, A. Subhan, S. N. Sari, A. S. Wismogroho, C. Hudaya and B. Prihandoko, Electrochemical performance of low concentration Al doped-lithium titanate anode synthesized via sol-gel for lithium ion capacitor applications, *J. Energy Storage*, 2020, **29**, 101480.

11 D. Qian, Y. Gu, Y. Chen, H. Liu, J. Wang and H. Zhou, Ultra-high specific capacity of Cr3 + -doped Li4Ti5O12 at 1.55 V as anode material for lithium-ion batteries, *Mater. Lett.*, 2019, **238**, 102–106.

12 S. Repp, E. Harputlu, S. Gurgen, M. Castellano, N. Kremer, N. Pompe, J. Wörner, A. Hoffmann, R. Thomann, F. M. Emen, S. Weber, K. Ocakoglu and E. Erdem, Synergetic effects of Fe^{3+} doped spinel $Li_4Ti_5O_{12}$ nanoparticles on reduced graphene oxide for high surface electrode hybrid supercapacitors, *Nanoscale*, 2018, **10**, 1877–1884.

13 H. Zou, X. Liang, X. Feng and H. Xiang, Chromium-Modified $Li_4Ti_5O_{12}$ with a Synergistic Effect of Bulk Doping, Surface Coating, and Size Reducing, *ACS Appl. Mater. Interfaces*, 2016, **8**, 21407–21416.

14 K. L. Salvatore, M. N. Vila, G. Renderos, W. Li, L. M. Housel, X. Tong, S. C. McGuire, J. Gan, A. Paltis, K. Lee, K. J. Takeuchi, A. C. Marschilok, E. S. Takeuchi and S. S. Wong, Probing the Physicochemical Behavior of Variously Doped $Li_4Ti_5O_{12}$ Nanoflowers, *ACS Phys. Chem. Au*, 2022, **2**, 331–345.

15 Z. Xie, Q. Song, H. Xie, H. Yin and Z. Ning, Chemically driven synthesis of Ti^{3+} self-doped $Li_4Ti_5O_{12}$ spinel in molten salt, *J. Am. Ceram. Soc.*, 2021, **104**, 753–765.

16 K. Liang, H. He, Y. Ren, J. Luan, H. Wang, Y. Ren and X. Huang, Ti3+ self-doped Li4Ti5O12 with rich oxygen vacancies for advanced lithium-ion batteries, *Ionics*, 2020, **26**, 1739–1747.

17 G. Yang and S.-J. Park, Single-step solid-state synthesis and characterization of $Li_4Ti_{5-x}Fe_xO_{12-y}$ ($0 \leq x \leq 0.1$) as an anode for lithium-ion batteries, *J. Mater. Chem. A*, 2020, **8**, 2627–2636.

18 K. L. Salvatore, D. M. Lutz, H. Guo, S. Yue, J. Gan, X. Tong, P. Liu, E. S. Takeuchi, K. J. Takeuchi, A. C. Marschilok and S. S. Wong, Solution-Based, Anion-Doping of $Li_4Ti_5O_{12}$ Nanoflowers for Lithium-Ion Battery Applications, *Chem. – Eur. J.*, 2020, **26**, 9389–9402.

19 M. Ding, H. Liu, J. Zhu, X. Zhao, L. Pang, Y. Qin and L. Deng, Constructing of hierarchical yolk-shell structure Li4Ti5O12-SnO2 composites for high rate lithium ion batteries, *Appl. Surf. Sci.*, 2018, **448**, 389–399.

20 C. Chen, X. Liu, C. Ai and Y. Wu, Enhanced lithium storage capability of Li 4 Ti 5 O 12 anode material with low content Ce modification, *J. Alloys Compd.*, 2017, **714**, 71–78.

21 X. Ji, D. Li, Q. Lu, E. Guo and L. Yao, Electrospinning preparation of one-dimensional Ce3 + -doped Li4Ti5O12 sub-microbelts for high-performance lithium-ion batteries, *J. Nanopart. Res.*, 2017, **19**, 393.

22 H. Kim, D. Kim, K. Hara, H. Shiiba, Y. Charles-Blin, E. Otal, H. Tanaka, K. Teshima, G. Sánchez-Santolino, R. Ishikawa, Y. Ikuhara and N. Zettsu, Mixed anion effects on structural and electrochemical characteristics of $Li_4Ti_5O_{12}$ for high-rate and durable anode materials, *J. Mater. Chem. A*, 2024, **12**, 7107–7121.

23 S. Saxena and A. Sil, Role of calcination atmosphere in vanadium doped Li 4 Ti 5 O 12 for lithium ion battery anode material, *Mater. Res. Bull.*, 2017, **96**, 449–457.

24 T. Subburaj, K. Prasanna, K. J. Kim, P. R. Ilango, Y. N. Jo and C. W. Lee, Structural and electrochemical evaluation of bismuth doped lithium titanium oxides for lithium ion batteries, *J. Power Sources*, 2015, **280**, 23–29.

25 G. Yang and S.-J. Park, The formation mechanism of Li4Ti5O12−y solid solutions prepared by carbothermal

reduction and the effect of Ti3+ on electrochemical performance, *Sci. Rep.*, 2019, **9**, 4774.

26 A. Mahmoud, J. M. Amarilla, K. Lasri and I. Saadoune, Influence of the synthesis method on the electrochemical properties of the Li4Ti5O12 spinel in Li-half and Li-ion full-cells. A systematic comparison, *Electrochim. Acta*, 2013, **93**, 163–172.

27 D. Aurbach, Y. Gofer, O. Chusid and H. Eshel, On nonaqueous electrochemical behavior of titanium and Ti4+ compounds, *Electrochim. Acta*, 2007, **52**, 2097–2101.

28 X. Ji, X. Dai, F. Wu and H. Jin, Liquid-Phase Integrated Surface Modification to Construct Stable Interfaces and Superior Performance of High-Voltage $LiNi_{0.5}Mn_{1.5}O_4$ Cathode Materials, *ACS Sustainable Chem. Eng.*, 2022, **10**, 9850–9859.

29 W. Li, X. Li, M. Chen, Z. Xie, J. Zhang, S. Dong and M. Qu, AlF_3 modification to suppress the gas generation of $Li_4Ti_5O_{12}$ anode battery, *Electrochim. Acta*, 2014, **139**, 104–110.

30 N. Nzimande, A. Haruna, P. Mwonga, B. Rasche, F. Cummings and K. I. Ozoemena, Ceria-Spiderweb Nanosheets Unlock the Energy-Storage Properties in the "Sleeping" Triplite $(Mn_2(PO_4)F)$, *ACS Appl. Energy Mater.*, 2021, **4**, 13085–13097.

31 A. B. Haruna, D. H. Barrett, C. B. Rodella, R. M. Erasmus, A. M. Venter, Z. N. Sentsho and K. I. Ozoemena, Microwave irradiation suppresses the Jahn-Teller distortion in Spinel LiMn2O4 cathode material for lithium-ion batteries, *Electrochim. Acta*, 2022, **426**, 140786.

32 J. Yoon, S. Nam, H. Shim, K. Park, T. Yoon, H. Park and S. Hyun, Highly-Stable Li4Ti5O12 Anodes Obtained by Atomic-Layer-Deposited Al2O3, *Materials*, 2018, **11**, 803.

33 J. Rikarte, B. Acebedo, A. Vilalta-Clemente, F. Bonilla, A. J. Wilkinson, M. Galceran, A. Lousa, J. Rubio-Zuazo and M. Á. Muñoz-Márquez, Surface Evolution of Lithium Titanate upon Electrochemical Cycling Using a Combination of Surface Specific Characterization Techniques, *Adv. Mater. Interfaces*, 2020, **7**, 1902164.

34 M. Qin, Y. Li and X.-J. Lv, Preparation of Ce- and La-Doped Li4Ti5O12 Nanosheets and Their Electrochemical Performance in Li Half Cell and Li4Ti5O12/LiFePO4 Full Cell Batteries, *Nanomaterials*, 2017, **7**, 150.

35 S. Liu, Y. Hui, L. Zhu, X. Fan, B. Zou and X. Cao, Synthesis and luminescence properties of CeF3:Tb3+ nanodisks via ultrasound assisted ionic liquid method, *J. Rare Earths*, 2014, **32**, 508–513.

36 H. Zhang, P. Liu, F. Li, H. Liu, Y. Wang, S. Zhang, M. Guo, H. Cheng and H. Zhao, Facile Fabrication of Anatase TiO_2 Microspheres on Solid Substrates and Surface Crystal Facet Transformation from {001} to {101}, *Chem. – Eur. J.*, 2011, **17**, 5949–5957.

37 S. K. Jha, N. Nakamura, S. Zhang, L. Su, P. M. Smith, X. L. Phuah, H. Wang, H. Wang, J. S. Okasinski, A. J. H. McGaughey and B. Reeja-Jayan, Defect-Mediated Anisotropic Lattice Expansion in Ceramics as Evidence for Nonthermal Coupling between Electromagnetic Fields and Matter, *Adv. Eng. Mater.*, 2019, **21**, 1900762.

38 B. Vaidhyanathan, A. P. Singh, D. K. Agrawal, T. R. Shrout, R. Roy and S. Ganguly, Microwave Effects in Lead Zirconium Titanate Synthesis: Enhanced Kinetics and Changed Mechanisms, *J. Am. Ceram. Soc.*, 2001, **84**, 1197–1202.

39 N. M. Ncube, W. T. Mhlongo, R. I. McCrindle and H. Zheng, The electrochemical effect of Al-doping on Li 4 Ti 5 O 12 as anode material for lithium-ion batteries, *Mater. Today: Proc.*, 2018, **5**, 10592–10601.

40 H. A. Llaín-Jiménez, D. A. Buchberger, M. Winkowska-Struzik, M. Ratyński, M. Krajewski, M. Boczar, B. Hamankiewicz and A. Czerwiński, Correlation between Lithium Titanium Oxide Powder Morphology and High Rate Performance in Lithium-Ion Batteries, *Batteries*, 2022, **8**, 168.

41 T.-F. Yi, J. Shu, Y.-R. Zhu, X.-D. Zhu, C.-B. Yue, A.-N. Zhou and R.-S. Zhu, High-performance $Li_4Ti_{5-x}V_xO_{12}$ ($0 \leq x \leq 0.3$) as an anode material for secondary lithium-ion battery, *Electrochim. Acta*, 2009, **54**, 7464–7470.

42 J.-Y. Liao, V. Chabot, M. Gu, C. Wang, X. Xiao and Z. Chen, Dual phase Li4Ti5O12–TiO2 nanowire arrays as integrated anodes for high-rate lithium-ion batteries, *Nano Energy*, 2014, **9**, 383–391.

43 J. Kim, M. Park, S. M. Hwang, Y. Heo, T. Liao, Z. Sun, J. H. Park, K. J. Kim, G. Jeong, Y. Kim, J. H. Kim and S. X. Dou, Zr^{4+} Doping in $Li_4Ti_5O_{12}$ Anode for Lithium-Ion Batteries: Open Li^+ Diffusion Paths through Structural Imperfection, *ChemSusChem*, 2014, **7**, 1451–1457.

44 C. Wu, Y. Wang, G. Ma and X. Zheng, Enhanced rate capability of Li4Ti5O12 anode material by a photo-assisted sol–gel route for lithium-ion batteries, *Electrochem. Commun.*, 2021, **131**, 107119.

45 W. Qin, H. Liu, J. An and X. Wen, Enhanced Li-ion battery performance of TiO2 nanoparticle-loaded Li4Ti5O12 nanosheet anode using carbon coated copper as current collector, *J. Power Sources*, 2020, **479**, 229090.

46 L. Cheng, X.-L. Li, H.-J. Liu, H.-M. Xiong, P.-W. Zhang and Y.-Y. Xia, Carbon-Coated Li[sub 4]Ti[sub 5]O[sub 12] as a High Rate Electrode Material for Li-Ion Intercalation, *J. Electrochem. Soc.*, 2007, **154**, A692.

47 D. Li, Y. Liu, W. Zhao, Y. Gao, L. Cao, Y. Liu, W. Wang, L. Yi and T. Qi, Synthesis of Ce modified Li4Ti5O12 using biomass as carbon source, *J. Electroanal. Chem.*, 2019, **851**, 113441.

48 T.-F. Yi, J.-Z. Wu, M. Li, Y.-R. Zhu, Y. Xie and R.-S. Zhu, Enhanced fast charge–discharge performance of $Li_4Ti_5O_{12}$ as anode materials for lithium-ion batteries by Ce and CeO_2 modification using a facile method, *RSC Adv.*, 2015, **5**, 37367–37376.

49 A. Nozariasbmarz, K. Dsouza and D. Vashaee, Field induced decrystallization of silicon: Evidence of a microwave non-thermal effect, *Appl. Phys. Lett.*, 2018, **112**, 093103.

50 W. Yu and G. Shao, Morphology engineering of defective graphene for microwave absorption, *J. Colloid Interface Sci.*, 2023, **640**, 680–687.

51 E. Temeche, E. Buch, X. Zhang, T. Brandt, A. Hintennach and R. M. Laine, Improved Electrochemical Properties of $Li_4Ti_5O_{12}$ Nanopowders (NPs) via Addition of $LiAlO_2$ and Li_6SiON Polymer Electrolytes, Derived from Agricultural Waste, *ACS Appl. Energy Mater.*, 2021, **4**, 1894–1905.

52 S. U. Muzayanha, A. Purwanto, M. I. Putra and H. K. Aliwarga, The Effect of Modified LTO Synthesis using Salt Assisted Method with Various of Salt Metal Materials, *IOP Conf. Ser.:Mater. Sci. Eng.*, 2021, **1117**, 012022.

53 Y. Zhang, M. Zeng, X. Wu, Y. Bai and J. Li, Solvothermal synthesis method for dual-phase $Li_4Ti_5O_{12}/TiO_2$ composites for high-stability lithium storage, *Mater. Res. Express*, 2020, **7**, 015515.

54 L. Noerochim, W. Caesarendra, A. Habib, Widyastuti, Suwarno, Y. L. Ni'mah, A. Subhan, B. Prihandoko and B. Kosasih, Role of TiO2 Phase Composition Tuned by LiOH on The Electrochemical Performance of Dual-Phase Li4Ti5O12-TiO2 Microrod as an Anode for Lithium-Ion Battery, *Energies*, 2020, **13**, 5251.

55 P. Ghasemiahangarani, G. Farhan, D. Del Mundo and T. Schoetz, Charge Storage Mechanisms in Batteries and Capacitors: A Perspective of the Electrochemical Interface, *Adv. Energy Mater.*, 2025, **15**, 2404704.

56 J. H. Jeong, B.-H. Park, G.-W. Lee, K. C. Roh and K.-B. Kim, Phase transformation of spinel Li4Ti5O12 to anatase TiO2 by catalytic delithiation, *Energy Storage Mater.*, 2020, **25**, 510–519.

57 Y. Wei, K. Tuo, P. Wang, L. Yang, W. Liang, H. Ding, X. Cui and S. Li, Appropriate proportion truncated octahedron LiNi0.5Mn1.5O4 with excellent electrochemical properties for lithium-ion batteries prepared by graphite-assisted calcination method, *Ionics*, 2020, **26**, 6003–6012.

58 C. Chen, R. Agrawal and C. Wang, High Performance Li4Ti5O12/Si Composite Anodes for Li-Ion Batteries, *Nanomaterials*, 2015, **5**, 1469–1480.

59 C. Y. Bon, P. Isheunesu, S. Kim, M. Manasi, Y. I. Kim, Y. J. Lee and J. M. Ko, High Capacity and Fast Charge-Discharge $Li_4Ti_5O_{12}$ Nanoflakes/TiO_2 Nanotubes Composite Anode Material for Lithium Ion Batteries, *Energy Technol.*, 2018, **6**, 2461–2468.

60 D. M. Cunha, T. A. Hendriks, A. Vasileiadis, C. M. Vos, T. Verhallen, D. P. Singh, M. Wagemaker and M. Huijben, Doubling Reversible Capacities in Epitaxial $Li_4Ti_5O_{12}$ Thin Film Anodes for Microbatteries, *ACS Appl. Energy Mater.*, 2019, **2**, 3410–3418.

61 A. Kazemi, R. Mostaani, M. K. Ravari, M. Ghorbanzadeh, M. Yavarinasab, J. Enferadi, Z. Chen, N. Iqbal, Y. Xiang, W. Liu and A. Davoodi, Enhancing high rate performance of Lithium Titanium Oxide (LTO) anodes: A comprehensive review, *J. Power Sources*, 2025, **630**, 236051.

62 A. B. Haruna, P. Mwonga, D. Barrett, C. B. Rodella, R. P. Forbes, A. Venter, Z. Sentsho, P. J. Fletcher, F. Marken and K. I. Ozoemena, Defect-Engineered β-$MnO_{2-\delta}$ Precursors Control the Structure–Property Relationships in High-Voltage Spinel $LiMn_{1.5}Ni_{0.5}O_{4-\delta}$, *ACS Omega*, 2021, **6**, 25562–25573.

63 Y. Yin, X. Luo and B. Xu, In-situ self-assembly synthesis of low-cost, long-life, shape-controllable spherical Li4Ti5O12 anode material for Li-ion batteries, *J. Alloys Compd.*, 2022, **904**, 164026.

64 G. Wang, H. Wang, G. Ma, X. Du, L. Du, P. Jing, Y. Wang, K. Wu, H. Wu, Q. Wang and Y. Zhang, Investigation on process mechanism of a novel energy-saving synthesis for high performance Li4Ti5O12 anode material, *J. Energy Chem.*, 2022, **70**, 266–275.

65 G. Yan, X. Xu, W. Zhang, Z. Liu and W. Liu, Preparation and electrochemical performance of P^{5+}-doped $Li_4Ti_5O_{12}$ as anode material for lithium-ion batteries, *Nanotechnology*, 2020, **31**, 205402.

66 M. Shen, J. Zhu, S. Sun, D. Chen, F. Liu and J. Chen, Theoretical Prediction and Experimentally Realizing Cathodic Doping of Sulfur in $Li_4Ti_5O_{12}$ for Superior Lithium Storage Performance, *ACS Appl. Energy Mater.*, 2021, **4**, 5995–6004.

67 X. Xiao, L. Liu, L. Zhang, Q. Wang, H. Yan, B. Zhao, L. Wang, L. Ma, Y. Liu and H. An, Electrochemical and transport properties of Te-doped Li4Ti5O12 as anode material for lithium-ion half/full batteries, *J. Alloys Compd.*, 2022, **897**, 162744.

68 D. Qian, Y. Gu, S. Guo, H. Liu, Y. Chen, J. Wang, G. Ma and C. Wu, Effect of rich R-TiO2 on the rate and cycle properties of Li4Ti5O12 as anode for lithium ion batteries, *J. Energy Chem.*, 2019, **32**, 182–188.

69 Y. Zhang, Y. Zhang, L. Huang, Z. Zhou, J. Wang, H. Liu and H. Wu, Hierarchical carambola-like Li4Ti5O12-TiO2 composites as advanced anode materials for lithium-ion batteries, *Electrochim. Acta*, 2016, **195**, 124–133.